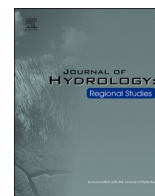


Contents lists available at [ScienceDirect](https://www.sciencedirect.com)

Journal of Hydrology: Regional Studies

journal homepage: www.elsevier.com/locate/ejrh

Rainfall erosivity across Austria's main agricultural areas: Identification of rainfall characteristics and spatiotemporal patterns

Cristina Vásquez^{a,*}, Andreas Klik^a, Christine Stumpp^a, Gregor Laaha^c, Peter Strauss^b, Nur Banu Özcelik^c, Georg Pistotnik^d, Shuiqing Yin^e, Tomas Dostal^f, Gabriel Gaona^g, Stefan Strohmeier^a

^a University of Natural Resources and Life Sciences, Institute of Soil Physics and Rural Water Management, Vienna, Austria

^b Federal Agency for Water Management Institute for Land and Water Management Research, Petzenkirchen, Austria

^c University of Natural Resources and Life Sciences, Institute of Statistics, Vienna, Austria

^d Zentralanstalt für Meteorologie und Geodynamik, Vienna, Austria

^e State Key Laboratory of Earth Surface Processes and Resource Ecology, Faculty of Geographical Science, Beijing Normal University, Beijing, China

^f Faculty of Civil Engineering, Czech Technical University in Prague, Prague, Czech Republic

^g Laboratorio de servicios hidrometeorológicos, Grupo de Recursos Hídricos y Acuáticos, Universidad Regional Amazónica Ikiam, Tena, Ecuador

ARTICLE INFO

Keywords:

Rainfall erosivity

Spatiotemporal erosivity

Agricultural areas

Erosive rainfall patterns

Clustering analysis

ABSTRACT

Study region: Target area of this study are the main agricultural production zones of Austria. Most important croplands cover the flat to pre-alpine areas concentrated in the north, east, and southeast of Austria.

Study focus: The novelty of our study is the spatiotemporal assessment of rainfall characteristics that drive erosivity at the event level as well as the identification of erosive rainfall distribution patterns within the events. Our assessment approach allows the definition of both typical and extreme erosivity. Long-term and high temporal resolution rainfall datasets were used to apply a clustering approach, seasonal and spatial analyses, and rainfall distributions assessment (isopleths) of the identified rainfall types (clusters).

New hydrological insights for the region: Three dominant erosive event-types (clusters) were identified that strongly relate with Austria's seasonality and complex topography. The most erosive rainfall events (cluster C1) are characterized by a high intensity and short duration. C1 events have the largest occurrence frequency in pre-alpine southern Austria and occur from May to September. Unlike the less erosive and more evenly distributed event types (C2 and C3) the highly erosive C1 events have a pronounced maximum rainfall intensity at the onset of the event.

1. Introduction

Natural phenomena, such as unusual rain and wind storms (Azimzadeh et al., 2022; Marzen et al., 2017), overlaid with intensive agricultural management (e.g. removal of native vegetation and frequent soil tillage), can generate severe soil erosion, threaten soil health, and lead to the degradation of biodiversity and the reduction of the crop production potential (Borrelli et al., 2022; Panagos

* Corresponding author.

E-mail address: cristina.vasquez-ojeda@boku.ac.at (C. Vásquez).

<https://doi.org/10.1016/j.ejrh.2024.101770>

Received 24 December 2023; Received in revised form 25 March 2024; Accepted 29 March 2024

Available online 4 April 2024

2214-5818/© 2024 The Authors. Published by Elsevier B.V. This is an open access article under the CC BY license (<http://creativecommons.org/licenses/by/4.0/>).

et al., 2016). According to the Thematic Strategy for Soil Protection in European Union (EU) (European Commission – Soil Thematic Strategy, 2006), soil erosion by water is a top-ranked hazard for soils in Europe (Panagos et al., 2016; Panagos and Katsoyiannis, 2019). Borrelli et al. (2022) found high soil erosion rates occurring over half of the European Union's arable land (53.7%), where soil displacement due to rainfall is estimated to account for 51% of the total soil displacement.

The rainfall erosivity factor (R) used in the Universal Soil Loss Equation (USLE) and Revised Universal Soil Loss Equation (RUSLE) models (Renard et al., 1991) includes the kinetic energy of rainfall as well as the 30-minute maximum intensity (EI_{30}) to account for both, the erosive power of raindrops and the potential surface runoff that transports the detached soil particles. The according rainfall erosivity factor (EI_{30}) is one of the most commonly applied indicators used to define the erosive potential of a storm and combines the effects of precipitation duration, amount, and intensity (Lai et al., 2016; Renard et al., 1991). Rainfall erosivity can greatly vary between rainfall events even within a geographic area (Lee et al., 2022). Rainfall erosivity variation is largely determined by the spatiotemporal distribution of rainfall amounts, rainfall intensities, and seasonal characteristics (Schmidt et al., 2016). However, based on the traditional USLE-RUSLE approaches, where R-factors represent average erosivity conditions, and following the argument of Wischmeier and Smith (1958) that storm patterns exhibit random distributions over time, disregarding these patterns does not exert a notable impact on the long-term prediction of EI_{30} . From this perspective, extreme events are excluded ahead of calculations (Yin et al., 2017) or intense events should be treated as outliers and neglected for erosivity assessments (Padulano et al., 2021). Accordingly, and in simplified practical applications, the assessment of soil degradation commonly relies on average annual cumulative rainstorm erosivity values.

González-Hidalgo et al. (2007) and Bagarello et al. (2011) showed that infrequent extreme erosive events significantly impact soil loss. Studies by Bagarello et al. (2011) claim that a small number of infrequent, short-duration, but intense rainfall events can cause a majority of soil loss. González-Hidalgo et al. (2007), on a daily soil erosion study in Western Mediterranean areas, found that over 50% of the soil eroded annually was related to only three (daily) erosion events despite high variability between sites, years, and different approaches. Bagarello et al. (2011) claimed that approximately 75% of the annual soil loss measured at the plot scale on bare soil at the Sparacia (South Italy) experimental station was due to a single event. Long-term field plot observations in eastern Austria showed that the three most significant erosion events between 1994 and 2019 accounted for 79% of total soil loss during the same period (Klik and Rosner, 2020). Yang et al. (2022), using six years of data from the Mahuangtian Basin in China, found greater values of sediment yield and runoff in 2018 and 2019 than in other years due to extreme rainfall events. Peng and Dai (2022), after conducting rainfall experiments on simulated slopes with surface-exposed bedrock and subsurface fissures, found that rainfall intensity was the driving factor determining the amount of soil surface erosion and subsurface leakage loss.

As peak rainfall intensity could occur early in the storm, in the middle, or at the end (Nyssen et al., 2005), the intra-storm variation of peak rainfall intensity affects peak runoff rates, infiltration, and accordingly, soil erosion (Flanagan et al., 1988; Parsons and Stone, 2006). For example, Wang et al. (2016) analyzed the effects of different storm patterns (of constant rainfall amount) on soil loss under natural rainfall. The authors found that storms with peak intensities occurring during the first half of the duration generated the largest contribution (55–68%) to the total erosion among the four patterns. Often, the highly erosive (e.g. convective) rainfalls generate their maximum intensities at the beginning of a rainstorm; in South Africa, more than half the storms generate their maximum peak intensity within the first quartile of the duration of the storm, and 84% of the storms show maximum intensity within the first half (Nel, 2007). In Rio de Janeiro, Brazil, similar conditions were found: maximum peak intensity occurs during the first half of the event duration in 45.7% of the storms (Machado et al., 2008).

In addition to that globally increasing climatic variability, including the infrequent intensive rainfall events, may further accelerate rainfall erosivity (Burt and Weerasinghe, 2014). A recent study conducted by Padulano et al. (2023) found that in the Mediterranean area, especially in Italy, annual precipitation totals are expected to be unchanged in the future. However, at a monthly/seasonal level, the authors found great variability, with areas affected by a possible severe increase in soil erosion due to rainfall erosivity patterns changes. According to the IPCC (2023), heavy precipitation events have become more frequent, intense, and voluminous since 1950, and it is probable that such trends will continue into the 21st century. This may also apply to Austria: a recent study by Johannsen et al. (2022), using high temporal resolution and long-term precipitation time series to develop updated R-factors at different spatial and temporal scales, concluded greater R-factor values compared to the publications of Strauss et al. (1995) and Klik and Konecny (2012). Klik and Konecny (2012) analyzed the rainfall erosivity of 51 rainfall stations in northeastern Austria and found stations with significantly increasing trends in rainfall intensity, rainfall erosivity, and event occurrence.

Rainfall characteristics play a crucial role in soil erosion and have a direct impact on soil detachment, water infiltration, and overland flow (Peng and Wang, 2012). Yang et al. (2022) proved that different erosive rainfall patterns have varying impacts on runoff and sediment yield. Similar observations reported by Li et al., (2023). The authors carried out a study in Kars areas, where the soil loss was affected by different rainfall patterns in the field and laboratory.

To date, research endeavors have predominantly focused on the assessment of long-term annual averages of soil erosion rates, often based on simplified or long-term rainfall erosivity assumptions. Enhanced comprehension of erosive occurrences about temporal and spatial patterns and dynamics, with a particular emphasis on extreme events, assumes a position of paramount significance in the precise assessment of erosion risk and the formulation of targeted mitigation strategies to alleviate the impact on agricultural areas. This is supported by local studies conducted in Austria by e.g. Strohmeier et al. (2015), which indicated that different environmental contexts react differently to the contribution of rare and infrequent extreme events.

Our work aims to investigate the spatiotemporal occurrence of rainfall erosivity across the most important agricultural areas in Austria emphasizing on the dominant event-types. The specific aims are (i) to calculate rainfall characteristics, including the USLE R-factor using long-term and high temporal resolution (5 min) measured rainfall data, (ii) to characterize and cluster dominant erosive events types, and (iii) to evaluate key spatial and temporal patterns of erosive rainfall events across the Main Agricultural Production

Zones (MAPZ) in Austria. The results of this study can be used to determine typical to extreme rainfall erosivity occurrences in space and time, which will subsequently support the development and design of well-tailored agricultural adaptation measures per context.

2. Materials and methods

2.1. Study area and rainfall data

Austria is characterized by a heterogenic topography due to the wide altitudinal range from the flatlands in the East, less than 250 m above sea level (a.s.l.), to more than 3500 m.a.s.l. along the Alpine ridge in the center and west (Matulla et al., 2003). Austria's climate is modulated by Atlantic influences from the west, Mediterranean influences from the south, and continental influences from the east, and shows large differences between the summer and winter seasons (Seibert et al., 2007). Annual precipitation varies between 430 mm in the eastern flatlands up to 2250 mm along the northern and southern Alpine rims, with an overall mean of 1170 mm (Matulla et al., 2003). The seasons include winter from December to February, spring from March to May, summer from June to August, and autumn from September to November.

Target of this study are the areas of greatest agricultural production in Austria. These croplands are predominantly concentrated in the north, east and southeast (Schmaltz et al., 2023). Austria was officially divided into eight agricultural production zones by the Federal Institute for Agriculture and Mountain Farmers' Issues.

(https://bab.gv.at/index.php?option=com_rsfiles&folder=Raumgliederungen/&Itemid=477&lang=de). This is also aligned with publications of the Federal Office for Water Management (BAW), such as Johannsen et al. (2022) and Schmaltz et al. (2023). The delimitation criteria were altitude, slope, the type and size of business, climate, soil characteristics, agricultural production, and land use. These areas were determined by High Alps (HA), Eastern Alps (AOR), Pre-Alps (VA), Waldviertel and Mühviertel (WMV), Alpine foothills (AVL), North eastern lowlands (NFH) and South eastern hills (SFH) and Carinthian basin (KB) (Fig. 1). The High Alps, a mountainous zone mostly covered by forest and grasslands with few cropland areas, was not considered in this study due to its minor agricultural importance. A total of 27 exceptionally long operating and adequate data-quality rainfall stations were selected and distributed across our target agricultural production zones. Each station recorded rainfall at 5-minute intervals and 0.1 mm resolution over periods ranging from 27 to 78 years. All data was provided and quality-controlled by the Federal Ministry of Agriculture, Forestry, Regions and Water Management of Austria. Daily temperature and snow accumulation data were used to distinguish snowfall from

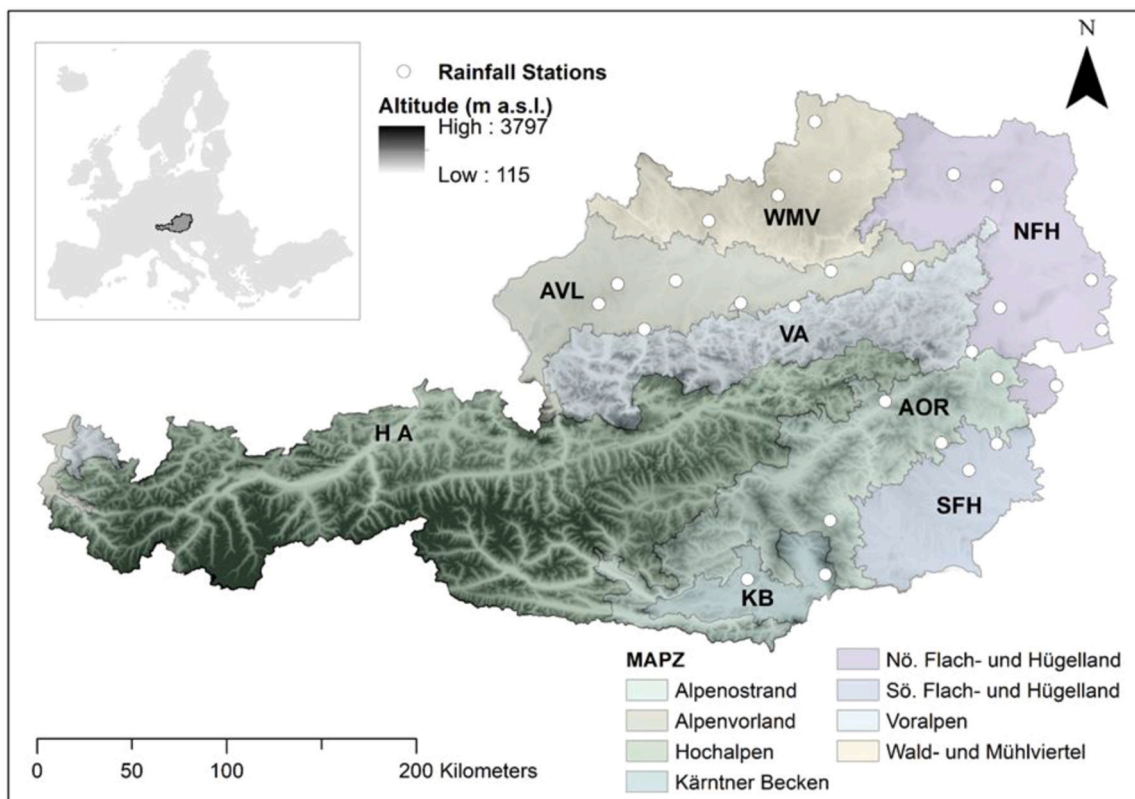


Fig. 1. Map of Austria's Main Agricultural Productions Zones and the distribution of selected rainfall stations. Eastern Alps, AOR; Alpine foothills, AVL; High Alps, HA; Carinthian basin, KB; NFH, North eastern lowlands, NFH; South eastern hills, SFH; Pre-Alps, VA; Waldviertel and Mühviertel, WMV.

rain events. A total of twenty-four stations with snow data and three stations with temperature data were assessed in this study. The details of stations within MAPZ are shown in Table 1 and Fig. 1.

2.2. Erosive rainfall characteristics and R-factor

The R-factor is the product of the kinetic energy of a rainfall event (E) and the maximum rainfall intensity within 30 min (I_{30}) (Wischmeier and Smith, 1958) for all rain events occurring during one year. Align with widely used US erosivity tools and models rainfall of less than 1.27 mm in six hours was used to separate events (Renard et al., 1991). Considering the central European context of our study, only rainfall events exceeding 10 mm were considered potentially erosive according to the definition of Rogler and Schwertmann (1981). The kinetic energy of each rainfall event was calculated based on the universal equation by Van Dijk et al. (2002) verified as producing reliable results across Austrian agricultural areas (Johannsen et al., 2022). The rainfall energy per unit depth for each time increment (e_r) was determined based on Eq. 1:

$$e_r = 0.0283(1 - 0.52 * \exp(0.042 * i_r)) \quad (1)$$

where i_r is rainfall intensity (mm h^{-1}) within the period r .

Total event kinetic energy for a single rainfall event (E_i) was then calculated by multiplying the rainfall energy per unit depth for each time increment (e_r) by the total depth during that increment (ΔV_r) and summing over the entire rain event:

$$E_i = \sum_{r=1}^0 e_r \Delta V_r \quad (2)$$

where 0 is the number of increments for the particular rain event.

The R-factor was calculated by summing the products of the total kinetic energy, E , and the maximum I_{30} for all events during n number of years:

$$R = \frac{1}{n} \sum_{j=1}^n \left[\sum_{k=1}^{mj} (EI_{30})_k \right] \quad (3)$$

Where R is the average annual rainfall erosivity ($\text{MJ mm ha}^{-1} \text{h}^{-1} \text{yr}^{-1}$), E in MJ ha^{-1} , I_{30} in mm h^{-1} , k is the index of number of erosive events in each year, m_j is the number of erosive events of a given year j , m is the number of events in each year, j is the index of the number of years used for average, and n is the number of years covered by the data period.

The erosivity density (ED) expresses the erosivity content per unit of rainfall. The event erosivity density is the ratio between the EI_{30} per event and the rainfall amount of erosive rainfall. It was calculated for all rainfall measurement stations. ED was also calculated

Table 1

Stations, data period, annual mean precipitation (P), Main Agricultural Productions Zones acronym and altitude of each rainfall station.

Station	Period	Years	P (mm)	Acronym	Altitude (m a.s.l.)
Altmanns	1977–2022	37	925	WMV	590
Hellmonsöd	1984–2022	39	746	WMV	840
Zwettl-Edelhof	1983–2022	39	607	WMV	595
Liebenau	1984–2022	39	483	WMV	953
Naglern	1981–2022	42	758	NFH	281
Andau	1980–2016	37	468	NFH	119
Blumau	1976–2017	42	735	NFH	233
Gattendorf	1964–2022	56	625	NFH	150
Hollabrunn	1984–2022	38	610	NFH	236
Neunkirchen	1976–2022	47	802	NFH	361
Nikitsch	1985–2022	34	512	NFH	222
Bad Waltersdorf	1965–2021	39	866	SFH	285
Pöllau	1979–2021	42	509	SFH	420
Oberwart	1956–2022	42	710	SFH	314
Behamberg	1978–2022	45	385	AVL	495
Geboltskirchen	1981–2022	42	514	AVL	540
Pyhra	1980–2022	41	710	AVL	298
Petzenkirchen	1937–2019	82	923	AVL	258
Bleistätter Moor	1946–2022	59	633	AVL	510
Frankenburg	1967–2022	55	720	AVL	515
Brandl Koralpe	1986–2022	27	830	KB	1415
Magdalensberg	1980–2022	40	720	KB	922
Gmunden Traundorf	1979–2022	44	701	VA	456
St.Leonhard am Walde	1979–2022	36	633	VA	634
Hollenthon	1978–2022	41	470	AOR	685
Kindtal	1968–2021	29	548	AOR	573
Packer Sperre	1954–2021	51	633	AOR	850

as the long-term mean R-factor divided by long-term mean rainfall by Eq.4:

$$ED = \left(\frac{R}{P} \right) \quad (4)$$

Where R is the average annual rainfall erosivity ($\text{MJ mm ha}^{-1} \text{ h}^{-1} \text{ yr}^{-1}$), and P is the average annual rainfall (mm yr^{-1}).

2.3. Event-based cluster analysis

Clustering of rainfall events was performed using the k-means algorithm (Lloyd, 1982). For this purpose, rainfall characteristics that drive erosivity i.e. rainfall amount, event duration and peak intensity (I_{30}) were used as input. All applied features were standardized for calculating the Euclidean distance. The optimum k-value was defined using the elbow method (Mouton et al., 2020), minimizing the prediction error while increasing the k-value (Syakur et al., 2018). The cluster analysis treats each sample as an object with a certain location in space. It finds a partition in which objects within each cluster are as close to each other and as far from objects in other clusters as possible. Eventually, each cluster is represented with a cluster centroid in the feature space. Using Euclidean distance, the distance between the samples and the cluster centroids is computed where the sum of distances from all objects in that cluster is minimized (Eq.5).

$$dist(Eucl) = \sum_{j=1}^k \sum_{i=1}^n (x_i - c_j)^2 \quad (5)$$

x_i is each data point, and c_j is the centroid of the cluster. The k-means algorithm is iterative; the process is repeated until the Euclidean distance converges to the minimum value. The Kolmogorov Smirnov test was applied to identify whether the variables are normally distributed or not. Once the Kolmogorov Smirnov test showed that the observations of each variable of the clusters were not normally distributed, Wilcoxon-Mann-Whitney-Test nonparametric method was applied to evaluate the dissimilarity between the clusters.

In addition, the spatial autocorrelation of the clusters within MAPZ was assessed. The Moran's I indices were applied to examine spatial autocorrelation patterns of erosive events per cluster. This study used the Global Moran's and the Local Moran's I index (MORAN, 1950) as local indicator of spatial association (LISA). Global measures characterize the nature of autocorrelation for the entire study area based on one single value that summarizes the average data behaviour. Local measures characterize spatial autocorrelation in extreme values concerning the mean, thereby helping identify hot spots (Anselin, 1995). Local Moran's I offers 4 types of results: high values in a high-value neighbourhood - high-high (HH) clusters, low values in a low-value neighbourhood - low-low (LL) clusters, a low value in a high-value neighbourhood - low-high (LH) and no spatial autocorrelation (zero values) marked as not significance. Moran's I values may be positive or negative, representing positive or negative spatial autocorrelation, respectively.

2.4. Sub-event level rainfall distribution

A modified 'Huff curve' (Huff, 1967) approach was applied to generate dimensionless cumulative hyetographs with specified probabilities of occurrence (Gordji et al., 2020; Bonta, 2004). For the modified Huff curve procedure the following steps were applied: 1) erosive rainfall events were defined and selected according to previous analyses; 2) per each event, total rainfall depth (A, mm), total duration (D, min), cumulative rainfall depth for the r th minute (A_r, mm), and cumulative duration for the r th minute (D_r, min) were obtained. 3) each event was dimensionless by dividing the cumulative rainfall amount (depth) by the total rainfall amount and dividing the cumulative duration by the total event duration;

$$p_r = \frac{A_r}{A} \quad (6)$$

$$t_r = \frac{D_r}{D} \quad (7)$$

for each event, values of $t_r = j$ ($j = 0, 0.1, 0.2, \dots, 0.8, 0.9, 1$) are identified or interpolated from the data with corresponding values of $p_j = p_r$. The value of p_j represents the dimensional cumulative rainfall depth at dimensional time j in the event.

4) for each value of j ($j = 0, 0.1, 0.2, \dots, 0.8, 0.9$), the n number of p_j values are sorted in descending order to obtain a series $(p_j)_i$ ($i = 1, 2, \dots, n$). 5) from this series, the empirical probability of exceedance value, $f(\%)$, for any value of $(p_j)_i$ is calculated as:

$$f = \frac{100i}{n+1} \quad (8)$$

$$i(f) = \left\lceil \frac{f(n+1)}{100} \right\rceil \quad (9)$$

The value of $(p_j)_{i(f)}$ for exceedance probabilities ($f = 10, 20, \dots, 80, 90$) was determined with Eqs. 8–9, same process for each of the nine values of j ($j = 0.1, 0.2, \dots, 0.8, 0.9$) was applied. For each value of f ($f = 10, 20, \dots, 80, 90$), a curve was drawn (isopleth) connecting

points j , $(p_j)_{i(f)}$. These isopleths derived in 10% increments from 10% to 90% and represent a set of Huff curves. The isopleths are a probabilistic summary representation of storm curves in terms of dimensionless elapsed times during an event and corresponding dimensionless cumulative rainfall amounts. For example, a 90% isopleth implies that for all event durations, 90% of the accumulated rainfall has occurred for all dimensionless event durations (Bonta, 2004). Three isopleths of 10%, 50%, and 90% are eventually presented in our research. The Huff curve approach was performed for each cluster identified.

3. Results

3.1. Erosive rainfall characteristics and R-factor

In total, 21686 erosive rainfall events are identified in 27 rainfall stations within the target MAPZ, with an average occurrence of 18 erosive events per year. The mean R-factor calculated for all rainfall stations is $1072 \text{ MJ mm ha}^{-1} \text{ h}^{-1} \text{ yr}^{-1}$ with a standard deviation of $376 \text{ MJ mm ha}^{-1} \text{ h}^{-1} \text{ yr}^{-1}$. R-factor ranges between $353 \text{ MJ mm ha}^{-1} \text{ h}^{-1} \text{ yr}^{-1}$ in Andau (NFH) in the east and $1833 \text{ MJ mm ha}^{-1} \text{ h}^{-1} \text{ yr}^{-1}$ in Pöllau (SFH) in the south (Table 2). At the event level, mean I_{30} is 10.5 mm h^{-1} , mean event duration is 18.6 h, and mean ED is around $2 \text{ MJ ha}^{-1} \text{ h}^{-1} \text{ yr}^{-1}$. The south-eastern pre-alpine areas, particularly in SFH, such as Bad Waltersdorf, and AOR, such as Kindtal, show the largest intensities with a mean annual maximum I_{30} of 44.3 mm h^{-1} and 47.2 mm h^{-1} , respectively. Furthermore, these sites are related to greater mean annual maximum ED and mean annual maximum event duration, but do not always show greater mean annual maximum rainfall amount. Rainfall stations within NFH, like Andau, are characterized by lowest mean annual maximum rainfall amount (40.6 mm), I_{30} (19.4 mm h^{-1}), and ED ($3.9 \text{ MJ ha}^{-1} \text{ h}^{-1} \text{ yr}^{-1}$). Stations within VA and AVL zones show greater mean annual maximum rainfall amounts; for instance, 84 mm in St Leonhard and 81 mm in Pyhra.

Table 3 presents the R-factor, erosivity density, and the according standard deviations per MAPZ. R-factors are generally greater in $\text{WMV} < \text{AVL} < \text{KB} < \text{VA} < \text{SFH} < \text{AOR}$ than NFH. Austria's southern MAPZ are characterized by the greatest mean maximum rainfall intensities as well as the greatest R-factor values and the largest standard deviation, except for the AOR zone, which has the lowest SD ($60 \text{ MJ mm ha}^{-1} \text{ h}^{-1} \text{ yr}^{-1}$). The erosive events of AOR with the greatest R-factor, $1514 \text{ MJ mm ha}^{-1} \text{ h}^{-1} \text{ yr}^{-1}$, and the second largest in ED have lower variance than KB and SHF zones. While the NFH zone in the East shows the lowest R-factor, mean maximum intensity, and mean maximum rainfall amount. In contrast, the northern zones, which also present large R-factor values, experience large rainfall amounts.

Table 2

Rainfall characteristics per station in the Main Agricultural Production Zones (MAPZ) of Austria. Location, number of events (>10 mm event precipitation), mean annual R-factor ($\text{MJ mm ha}^{-1} \text{ h}^{-1} \text{ yr}^{-1}$). At the event level, the mean of rainfall intensity I_{30} (mm h^{-1}), event duration EDur (h), and erosivity density ED ($\text{MJ ha}^{-1} \text{ h}^{-1}$). Mean annual maximum of rainfall amount (mm), EDur (h), rainfall intensity I_{30} (mm h^{-1}), and ED ($\text{MJ ha}^{-1} \text{ h}^{-1}$).

Station	Events	R-factor	I_{30}	EDur	ED	Mean annual event			
						Maximum rainfall amount	Maximum EDur	Maximum I_{30}	Maximum ED
Altmanns	545	820	8.9	18.9	1.7	59.0	45.8	33.4	7.6
Andau	453	353	7.5	15.0	1.3	40.6	40.8	19.4	3.9
Bad Waltersdorf	792	1417	12.6	20.0	2.6	52.2	62.5	44.3	10.9
Behamberg	1199	1074	7.9	20.6	1.4	73.5	56.6	29.8	6.7
Bleistätter Moor	1120	1071	10.5	20.4	2.0	56.6	53.0	33.3	7.8
Blumau	560	468	7.9	16.0	1.5	44.2	35.4	21.9	4.8
Brandl-Koralpe	664	1431	11.3	18.3	2.2	72.0	57.8	34.4	8.2
Frankenburg	1204	1253	10.8	21.8	2.1	70.5	59.9	39.4	9.4
Gattendorf	622	523	10.5	14.3	2.0	42.8	35.3	26.7	6.0
Geboltskirchen	940	1304	10.3	24.8	2.0	75.6	73.9	40.6	9.6
Gmunden-Traundorf	1089	1578	10.7	23.7	2.1	77.0	65.7	40.8	9.8
Hellmonsödt	713	1115	11.6	19.5	2.3	64.6	56.5	40.9	10.0
Hollabrunn	534	601	9.0	16.6	1.7	47.5	39.1	26.1	5.9
Hollenthon	809	1471	11.9	16.2	2.4	59.3	45.4	38.8	9.4
Kindtal	639	1489	12.0	22.5	2.5	55.4	82.2	47.2	11.5
Liebenau	649	1124	11.7	18.1	2.3	61.5	50.1	40.5	9.7
Magdalensberg	780	1025	10.1	17.4	1.9	56.5	54.1	32.2	7.5
Naglern	567	581	9.1	17.4	1.7	49.5	42.6	25.6	5.9
Neunkirchen	775	855	10.0	14.1	2.0	47.1	37.3	30.1	6.9
Nikitsch	515	882	11.6	14.5	2.3	44.4	37.1	32.7	7.5
Oberwart	729	1156	13.1	14.4	2.7	41.3	38.2	40.5	9.9
Packer Sperre	1112	1582	12.4	22.6	2.4	81.1	70.1	39.7	9.3
Petzenkirchen	1237	794	9.6	19.7	1.8	61.2	49.0	32.0	7.4
Pöllau (Zentralstation)	1005	1833	13.8	14.9	2.9	52.7	58.9	48.5	12.2
Pyhra	798	1104	9.4	18.9	1.8	81.3	49.1	32.0	7.4
St. Leonhard am Walde	968	1178	7.9	24.1	1.4	84.8	68.7	27.5	5.9
Zwettl Edelhof	668	890	10.5	17.6	2.1	54.9	48.8	34.5	8.1

Table 3

Mean annual R-factor ($\text{MJ mm ha}^{-1} \text{h}^{-1} \text{yr}^{-1}$) and standard deviation (SD); mean annual maximum of rainfall amount (mm) and rainfall intensity I_{30} (mm h^{-1}) within the Main Agricultural Production Zones (MAPZ) of Austria.

MAPZ	Region	R-factor	SD	Mean annual event	
				Maximum rainfall amount	Maximum I_{30}
WMV	N	987	155	60.0	37.3
AVL	N	1100	179	69.8	34.5
VA	N	1378	283	80.9	34.1
AOR	S	1514	59	65.2	41.9
KB	S	1228	287	64.2	33.3
SFH	S	1469	341	48.7	44.4
NFH	E	609	195	45.1	26.1

N: North, S: South, E: East.

3.2. Event-based cluster analysis

Three clusters of erosive events were identified with 2836, 15924, and 2926 events assigned to cluster one (C1), cluster two (C2), and cluster three (C3), respectively. The Kolmogorov Smirnov test showed a $p\text{-value} < 0.005$. The data is not normally distributed. Fig. 2 shows the cluster analysis input characteristics i.e. rainfall amount, I_{30} , and EDur as well as the clustered events' distributions of EI_{30} , ED. Overall, the most variable rainfall characteristics per cluster are EDur and rainfall amount. C1 contains the most erosive events with largest EI_{30} , I_{30} and ED values with a mean of $216 \text{ MJ mm ha}^{-1} \text{h}^{-1}$, 30.7 mm h^{-1} , and a mean of $7 \text{ MJ ha}^{-1} \text{h}^{-1}$, respectively. At the same time, C1 events are the shortest, with a mean EDur of about eight hours. C1 contains around 14% of the erosive events. C2 is characterized by events with the lowest mean EI_{30} ($21.8 \text{ MJ mm ha}^{-1} \text{h}^{-1}$) and lowest rainfall amount (17.3 mm). C2 events are the most frequent, accounting for 73% of total events. C3 event types represent 13% of total events, and their events

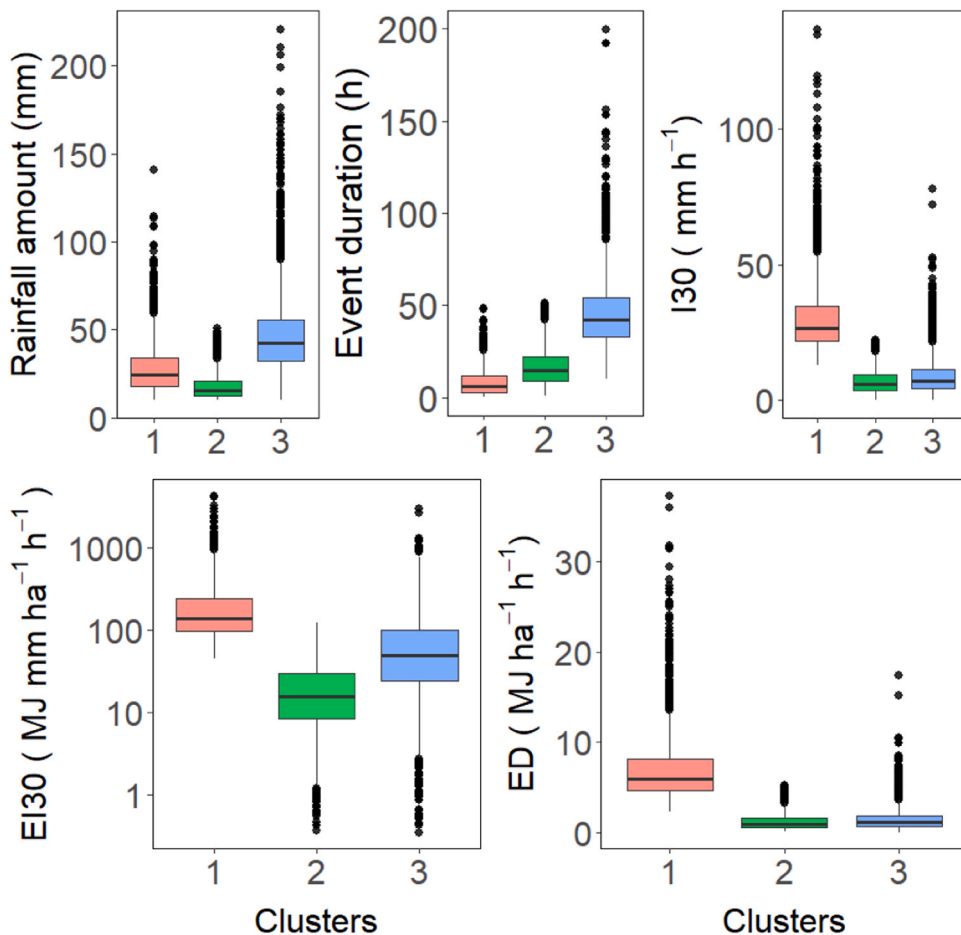


Fig. 2. Boxplots of EI_{30} , ED, and rainfall characteristics (I_{30} , EDur, rainfall amount) of three rainfall types/clusters (C1, C2, C3).

come along with the longest EDur and largest rainfall amount with mean values of 46 hours and 47.6 mm, respectively. Erosive events of C2 and C3 show similar mean values for ED ($1.22 \text{ MJ ha}^{-1} \text{ h}^{-1}$ and $1.48 \text{ MJ ha}^{-1} \text{ h}^{-1}$) and I_{30} (7.0 mm h^{-1} and 8.8 mm h^{-1}).

3.3. Spatial distribution of erosive rainfall events

Fig. 3 shows the spatial distribution of erosive events per cluster across MAPZ. Each pie chart indicates the percentage of the events per cluster, while the size of the pie chart represents the average annual number of highly erosive events (C1 type) per location. There is observed a greater occurrence of the most erosive events (C1) in the south-eastern pre-alpine areas (AOR and SHF) compared to the flatlands, particularly in the north-east of Austria. Using global and local Moran's I indices suggest a significant spatial autocorrelation of erosive rainfall events of all clusters (Table 4). This assessment provides evidence that the occurrence of erosive events is not only influenced by the local environment but also by other regional factors, for example the regional topography and climate, which supports a certain regionalization approach as applied through MAPZ. Local Moran's I shows the spatial autocorrelation patterns per each cluster (Figs. 4a-4c). Fig. 4a shows positive spatial autocorrelation of C1 events, particularly in the hot spot areas (high-high locations) in the south-eastern parts of the country where the most erosive rainfall events occur. On the contrary, 'low-low' C1 erosivity correlations are indicated in the flatlands in the northeast. Figs. 4b and 4c show the spatial patterns of the less erosive C2 and C3 events. 'High-high' locations are distributed in the northwest (AVL and VA), while 'low-low' locations are indicated in the east, mainly in NFH and in the eastern of AOR.

3.4. Temporal distribution of erosive rainfall events

3.4.1. Occurrence probability and intra-annual distribution

Figs. 5a and 5b show the empirical exceedance probability curves of rainfall amount and erosivity of all three clusters. In Fig. 5a, the curves C1–C3 reveal a large difference between the high and low erosive rainfall types concerning the total event precipitation amounts. The C2 curve contains events with a maximum rainfall amount of 50 mm, and only 5% of the events exceed 30 mm. On the other hand, more than 80% of C3 events have a total event precipitation amount $> 30 \text{ mm}$. Concerning rainfall amount, the most erosive events (C1) are evenly situated between the C2 and C3 lines. However, rainfall erosivity (EI_{30}) is by far largest in C1, as shown by the empirical exceedance probability curves in Fig. 5b. In C1, all events clearly exceed $90 \text{ MJ mm ha}^{-1} \text{ h}^{-1}$, and there is a probability of 10% that rainfall events may even exceed $500 \text{ MJ mm ha}^{-1} \text{ h}^{-1}$. In contrast, only a very low number of events of C3 reach $100 \text{ MJ mm ha}^{-1} \text{ h}^{-1}$.

Fig. 5c shows the seasonal distribution of rainfall erosivity. Overall, the largest number of erosive events, including the highly erosivity rainstorms (C1), occur during summer, and only a few erosive events occur in winter. Most highly erosive events occur from late spring (May) to early autumn (September). C2 events dominate the seasonal distribution throughout the year. In contrast, C3 events are more frequent during the summer season to early autumn and somewhat less frequent during the colder season from November to April.

3.4.2. Sub-event level rainfall distribution

To visualize the sub-event-level rainfall pattern and to compare typical distributions of the three defined clusters, isopleths of 10%, 50%, and 90% probability were plotted in Fig. 6. C1 isopleths have a predominately-pronounced maximum rainfall intensity at the onset of the event. For example, the isopleths of 50% and 90% indicate that approximately 0.6–0.9 of the cumulative event-rainfall

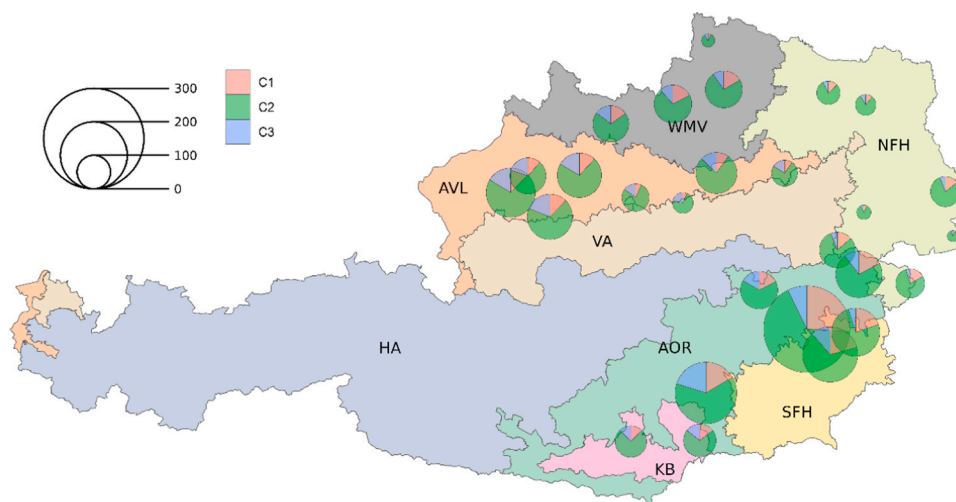


Fig. 3. Spatial distribution of erosive rainfall events per cluster. Each pie chart contains the clusters C1 to C3 and shows the percentage of events of each cluster. The pie chart's size relates to the number of events in C1.

Table 4
Global Moran's I statistics for each cluster shows spatial association in all clusters.

Cluster	Global Moran's I	P-value
1	0.279	0.004
2	0.350	0.002
3	0.552	0.000

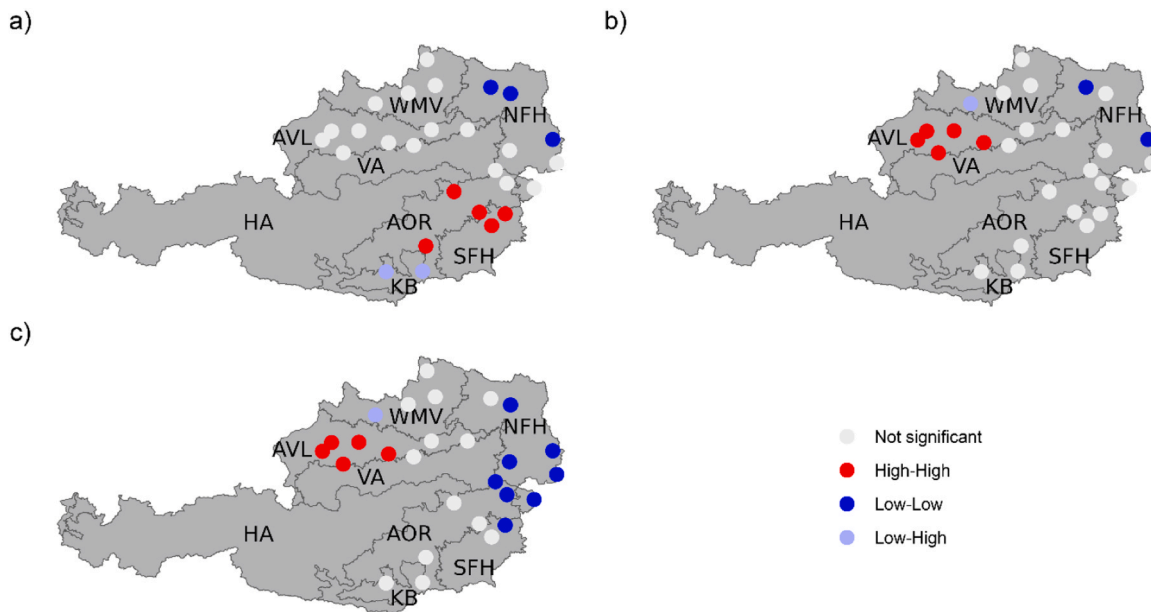


Fig. 4. Local Moran's I of spatial association of number of erosive events per cluster C1 (a), C2 (b) and C3 (c).

occurs within the first third of the rainfall duration. However, the 10% probability curve also unveils end-pronounced rainfall events in C1. Typically, C1 events have a rather steep rainfall depth increase – either beginning or end pronounced – which relates with high rainfall intensities. In contrast, C2 and C3 event types appear with a more uniform temporal rainfall distribution. Particularly, the 50% isopleths show a constant intensity over the entire event in both C2 and C3 clusters.

4. Discussion

A location's rainfall erosivity is controlled by the intensity and the occurrence frequency of extreme rainfall events. The present study, using extended period and high-resolution rainfall dataset, determines a substantial increase in rainfall erosivities in contrast to a study in the north-eastern part of Austria conducted by [Klik and Konecny \(2012\)](#) coinciding with eight stations. For example, the present study shows mean R-factor values in Blumau of 468, in Pyhra of 1104 or Gmunden with 1578 MJ mm ha⁻¹ h⁻¹ yr⁻¹. In addition, by MAPZ, values of 608, 1100, and 1378 MJ mm ha⁻¹ h⁻¹ yr⁻¹ for NFH, AVL, and VA, respectively. While, [Klik and Konecny \(2012\)](#) used a rainfall dataset at 15-minute time step and an average of 25 years to calculate R-factor. The authors found values of 273 for Blumau, of 766 for Pyhra and 1044 MJ mm ha⁻¹ h⁻¹ yr⁻¹ for Gmunden and 467 for NFH, 849 for AVL, and 1034 MJ mm ha⁻¹ h⁻¹ yr⁻¹ for VA. The datasets used by [Klik and Konecny \(2012\)](#) are shorter and already indicated increasing trends in erosivity in some of their assessed stations.

Our results are similar to those reported by [Johannsen et al. \(2022\)](#). Using a high temporal (5 minutes) and spatial resolution dataset, the authors calculated the R-factor from 1995 to 2015 in Austria. Nine of these stations were also used in the present study. Besides a possible trend over time and a time step that also impacts the quantification of rainfall erosivity using the USLE method ([Yue et al., 2022](#)). Different empirical considerations of the rainfall kinetic energy and intensity relationships (KE-I) can highly affect the erosivity estimation ([Nearing et al., 2017](#); [van Dijk et al., 2002](#)); our study is based on the equation of [Van Dijk et al. \(2002\)](#) as applied in the research conducted by [Johannsen et al. \(2022\)](#). Whereas, [Klik and Konecny \(2012\)](#) used the erosivity equation of [Brown and Foster \(1987\)](#).

The novelty of our study is the spatiotemporal assessment of factors that drive rainfall erosivity and the identification of their distribution-patterns at the event sub-event level. The clustering method detected three dominant erosive events, which are mainly determined by Austria's complex topography. Considering the central role of the Alps, the precipitation is influenced by three primary airflows, originating from the Atlantic, the Mediterranean, and Eastern Europe ([Matulla, 2003](#)). We found that the most frequently

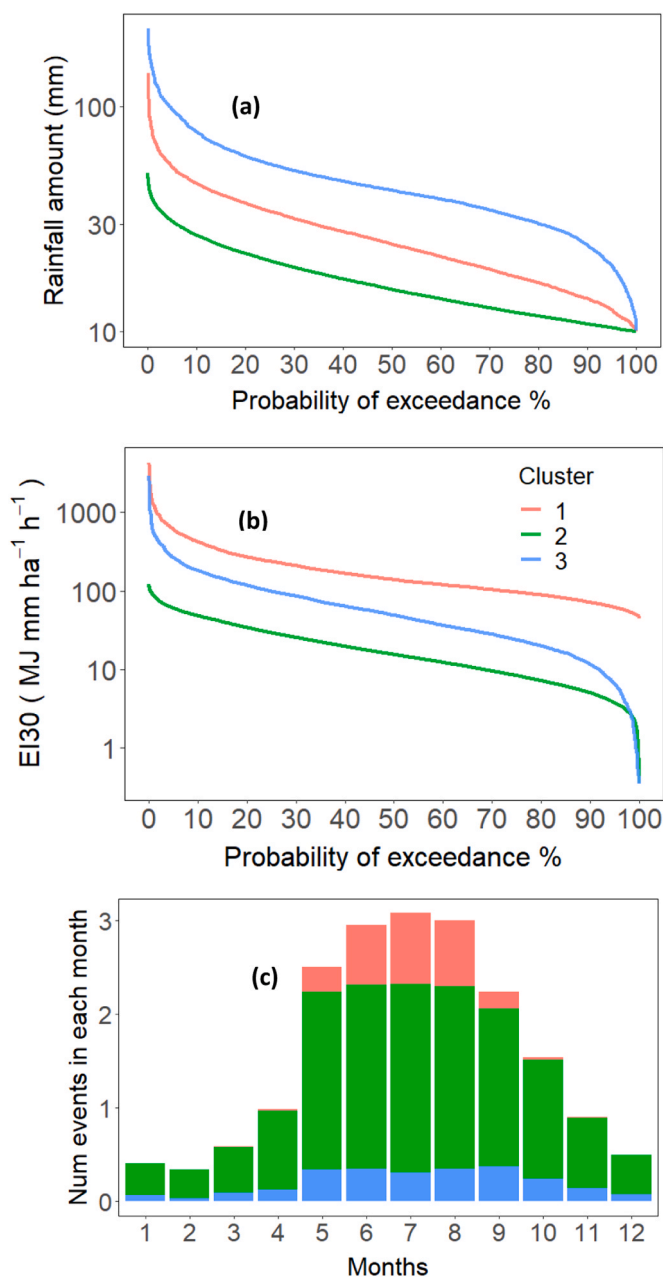


Fig. 5. Exceedance probability curves of rainfall amount (a) and EI₃₀ (b) per cluster; average number of erosive events (>10 mm) per cluster in the all period (c).

occurring rainfall event type in Austria, with more than 70% occurrence probability throughout the season (C2 events), is characterized by rather homogenous rainfall distributions, low intensities, and low rainfall amounts (Figs. 2 and 5a-b). Based on our applied criteria, these events have an average duration of 16 hours and are considered long duration, along with low values of EI₃₀.

According to the study by Seibert et al. (2007) these events could be related to very slow moving flows with approximately 3.8 m/s. Having the capacity to cause heavy rainfall everywhere in Austria with a minimum intensity in the northeast in addition to being relatively frequent.

A similar behavior of temporal rainfall distribution was observed for C3 events. However, these events are much longer, with an average duration of 46 hours. C3 events are characterized as large amounts of total event rainfall but mostly low to average intensities, contributing up to 13% of the erosive events within MAPZ.

These events could be given by flows that remain for a long time over the Atlantic Ocean, receiving strong humidification of the air, resulting more in longer rain events (sometimes multi-day) than convective storms. These events are more frequent in the north

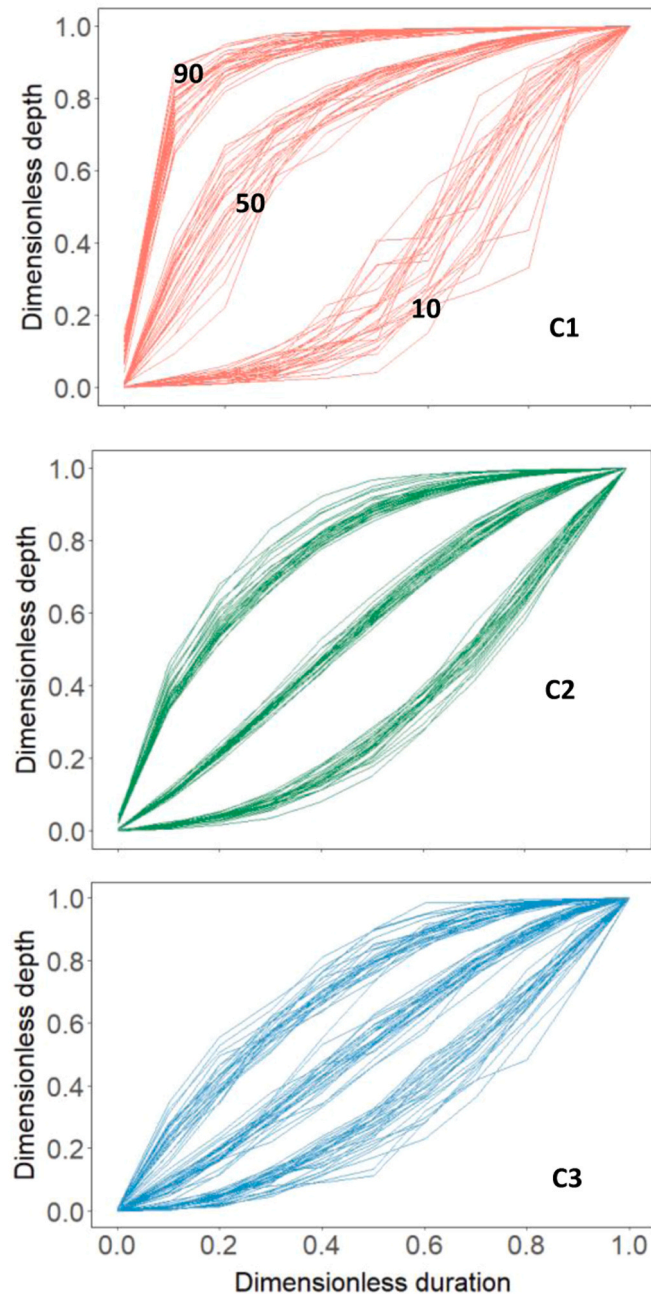


Fig. 6. Dimensionless cumulative distribution curves of normalized accumulated rainfall as a function of normalized progressive rainfall duration (Huff curves) per cluster and 10%, 50%, and 90% exceedance probabilities.

(Seibert et al., 2007).

Opposed to C2 and C3 events, the highly erosive C1 events mainly occur during summer time. They show the by far greatest EI_{30} values and have an average duration of 8 hours. At the sub-event-level more than 90% of rainfall occurs in the first hour the event. This in turn means that, commonly, less than 10% of the rainfall occurs with a low intensity at the tail-end of the C1 rainfall events.

In Austria, C1 erosive events appear to be dominated by convective processes that are more frequent in the zones closer to the Alpine areas. In the south, heavy rain events are most frequent (median values up to more than 50 mm), as they are additionally fed by the humidity of the Mediterranean when moist air masses from the south are steered towards the Alps, which was confirmed by an analysis with observed heavy precipitation in Austria (Seibert et al., 2007).

A strongly seasonal rainfall erosivity pattern was also observed in Italy (Padulano et al., 2023). Summer and autumn months were related with the largest average values: autumn was usually characterized by large cumulative rainfall, whereas in summer, rainfall

occurs through few high-intensity events.

In the southern hemisphere, in New Zealand, rainfall erosivity seemed largely controlled by climatic and topographic features. Lowest annual values ($<550 \text{ MJ mm ha}^{-1} \text{ h}^{-1}$) were observed in parts of Central Otago, and peak values ($>16\,000 \text{ MJ mm ha}^{-1} \text{ h}^{-1}$) in the Southern Alps. Seasonally, largest erosivity values occurred in December and January (southern summer), whereas the lowest values were observed in August (winter) (Klik et al., 2015). Identifying peak-periods and hotspots of erosivity eventually supports the soil erosion risk assessment in agriculture. The erosion risk of these areas is determined by the frequency with which the most erosive or extreme events occur. Fig. 4a determines that the highest risk agricultural areas identified as hot spots due to their high frequency of occurrence of erosive events are AOR and SFH and to a lesser extent KB.

Based on our study's spatiotemporal occurrence assessment of storm types and their most likely sub-event-level distributions, one or several representative or extreme rainstorms can be selected or generated per target location and seasonality as so-called 'design storm(s)'. Such design storms can be applied in subsequent modeling or artificial rainfall simulation experiments. Different rainfall intensities and temporal patterns interact with landscape characteristics and scales and eventually influence the catchment hydrology, such as flood peaks (Armon et al., 2019; Gao et al., 2018). While our actual research centers around the occurrence of rainfall erosivity as the driver of runoff and erosion, future research may facilitate those findings and relate spatio-temporal erosivity information with the catchment characteristics, e.g., adaptation to extreme runoff and sediment flows.

The gained knowledge on the driving rainfall erosion force and its' potential consequences (i.e. erosion modeling) can support a better targeted soil and water conservation design and implementation within the actual Austrian agriculture and climate context.

Nevertheless, upcoming changes in climate and according rainfall characteristics need to be carefully evaluated for the assessment of medium to long-term future erosivities. Increasing erosivity-trends in north-eastern Austrian MAPZ have been already reported by Klik and Konecny in 2012. Overall, major variations are expected in the total rainfall amount, duration, and mean rainfall intensity, as well as the frequency and intensity of extreme events (Papalexioiu and Montanari, 2019). Based on the Clausius-Clapeyron Law (i.e. a warmer atmosphere can hold more water vapor) an increase of 7% of rainfall intensity per $^{\circ}\text{C}$ is expected for physical reasons (Olefs et al., 2021). Even worse, Schroeer and Kirchengast (2018) found values of up to 14% rainfall intensity increase per $^{\circ}\text{C}$ based on 10-min records during days with extreme precipitation (98th percentile) in southeastern Austria, which clearly exceeds the theoretical value given by the Clausius-Clapeyron law. A future climate study for Italy showed that, on the seasonal level, large areas of the country might be affected by a possible severe increase of rainfall-induced soil erosion. Such an increase seems critical under the most optimistic scenario (RCP 2.6), whereas a potential increase might be lower under the most pessimistic scenarios (RCP 4.5 and 8.5) (Padulano et al., 2023). Rainfall erosivity is also expected to rise in most regions of China in both annual average rainfall erosivity (R-factor) and the extreme storm EI_{30} related with an e.g. 10-year return period which were primarily explained by the elevated probability of extreme precipitation events (Wang et al., 2023).

On the other hand, in a study by Riquetti et al. (2020) carried out in South America, the future projections were more pronounced in the Amazon Forest region, with a strong reduction in the mean annual precipitation and R-factor. The largest increase in the R-factor was projected for the Central and South Andes regions due to the increase in the mean annual precipitation.

According to the IPCC (2023), in most regions of Africa, Asia, North America, and Europe, at 1.5°C , global warming, heavy precipitation, and flooding events are projected to intensify and become more frequent. At 2°C or above, these changes expand to more regions and/or become more significant with severe agricultural and ecological droughts. As a general message: with increasing temperature extreme erosive events will likely increase. According future research and agricultural measures should investigate potential climate change implications on erosivity, building on the observations and thorough rainfall characteristics-erosivity assessments of historical data as performed in our present study.

5. Summary and Conclusions

This study used particularly long-term and high-temporal resolution rainfall datasets from 27 rainfall stations distributed across Austria's Main Agricultural Production Zones (MAPZ). A clustering analysis identified three dominant rainfall types (Clusters C1-C3) based on multiple rainfall characteristics related to erosivity (rainfall amount, intensity, and event duration). The study showed that the highly erosive C1 event-type is associated with particularly large rainfall intensities but short durations, while C2 and C3 events have longer durations, lower intensities and specifically lower rainfall erosivities. In contrast to that C3 events, mainly occurring in the northern pre-alpine areas, exceed the cumulative rainfall amount of C1 events. The highly erosive C1 events have a distinct spatial and temporal occurrence: our study unveils that zones closer to the High Alps (particularly south-eastern pre-alpine areas) have a larger occurrence frequency of C1 events, specifically during late spring, summer and early autumn, from May to September, which indicates a potential relationship with summer thunderstorms. At the sub-event-level, C1 storms reach their maximum intensity in the first fraction of the event. However, few C1 storms also come along with large rainfall intensities at the tail-end of the event. In contrast, the long-duration C2 and C3 events are rather evenly distributed concerning their cumulative rainfall amount.

Information on the event-types (clusters), their occurrence in space and time, as well as their rainfall distribution during the event (cumulative rainfall amount), enables the definition of typical and extreme rainfall events per location and target seasonality. This creates key input for advanced modelling studies and/or the conduction of specific and representative rainfall simulation experiments. The knowledge gained about the patterns of erosivity will provide crucial information for effectively planning and implementing adaptation strategies in the erosion-prone agricultural landscapes of Austria.

CRediT authorship contribution statement

Shuiqing Yin: Writing – review & editing. **Georg Pistotnik:** Writing – review & editing, Data curation. **Nur Banu Özcelik:** Writing – review & editing. **Gregor Laaha:** Writing – review & editing. **Peter Strauss:** Writing – review & editing, Supervision, Funding acquisition, Conceptualization. **Christine Stumpp:** Writing – review & editing. **Andreas Klik:** Writing – review & editing, Supervision, Funding acquisition, Conceptualization. **Cristina Vásquez:** Writing – review & editing, Writing – original draft, Visualization, Validation, Methodology, Investigation, Formal analysis, Data curation. **Stefan Strohmeier:** Writing – review & editing, Supervision, Project administration, Investigation, Formal analysis. **Gabriel Gaona:** Methodology, Data curation. **Tomas Dostal:** Writing – review & editing.

Declaration of Competing Interest

The authors declare that they have no known competing financial interests or personal relationships that could have appeared to influence the work reported in this paper.

Data Availability

Data will be made available on request.

Acknowledgments

This work was supported by the Climate and Energy Fund of the Austrian Federal Government ACRP13- EROS-A (No. KR20ACOK17974) and the National Key Research and Development Program of China (No. 2021YFE0113800).

References

- Anselin, L., 1995. Local Indicators of Spatial Association—LISA. *Geographical Analysis* 27 (2), 93–115. <https://doi.org/10.1111/j.1538-4632.1995.tb00338.x>.
- Armon, M., Morin, E., Enzel, Y., 2019. Overview of modern atmospheric patterns controlling rainfall and floods into the Dead Sea: implications for the lake's sedimentology and paleohydrology. *Quat. Sci. Rev.* 216, 58–73. <https://doi.org/10.1016/j.quascirev.2019.06.005>.
- Azimzadeh, H.R., Derakhshan, Z., Shirgahi, F., 2022. Field scale spatio-temporal variability of wind erosion transport capacity and soil loss at Urmia Lake. *Environ. Res.* 215 (P1), 114250 <https://doi.org/10.1016/j.envres.2022.114250>.
- Bagarello, V., Di Stefano, C., Ferro, V., Pampalona, V., 2011. Using plot soil loss distribution for soil conservation design. *CATENA* 86 (3), 172–177. <https://doi.org/10.1016/J.CATENA.2011.03.009>.
- Bonta, 2004. Development and Utility of Huff Curves for Disaggregating Precipitation Amounts. *Appl. Eng. Agric.* 20 (5), 641–653. <https://doi.org/10.13031/2013.17467>.
- Borrelli, P., Panagos, P., Alewell, C., Ballabio, C., de Oliveira Fagundes, H., Haregeweyn, N., Lugato, E., Maerker, M., Poesen, J., Vanmaercke, M., Robinson, D.A., 2022. Policy implications of multiple concurrent soil erosion processes in European farmland. *Nat. Sustain.* <https://doi.org/10.1038/s41893-022-00988-4>.
- Brown, L., Foster, G. R., 1987. Storm erosivity using idealized intensity distributions. *Trans. ASAE* 30 (2), 379. <https://doi.org/10.13031/2013.31957>.
- Burt, T., Weerasinghe, K., 2014. Rainfall distributions in Sri Lanka in time and space: an analysis based on daily rainfall data. *Climate* 2 (4), 242–263. <https://doi.org/10.3390/cli2040242>.
- Flanagan, D., Foster, G. R., Moldenhauer, W. C., 1988. Storm pattern effect on infiltration, runoff, and erosion. *Trans. ASAE* 31 (2), 414–420. <https://doi.org/10.13031/2013.30724>.
- Gao, J., Kirkby, M., Holden, J., 2018. The effect of interactions between rainfall patterns and land-cover change on flood peaks in upland peatlands. *J. Hydrol.* 567, 546–559. <https://doi.org/10.1016/j.jhydrol.2018.10.039>.
- González-Hidalgo, J.C., Peña-Monné, J.L., de Luis, M., 2007. A review of daily soil erosion in Western Mediterranean areas. *Catena* 71 (2), 193–199. <https://doi.org/10.1016/J.CATENA.2007.03.005>.
- Gordji, L., Bonta, J.V., Altinakar, M.S., 2020. Climate-related trends of within-storm intensities using dimensionless temporal-storm distributions. *J. Hydrol. Eng.* 25 (5), 1–13. [https://doi.org/10.1061/\(asce\)he.1943-5584.0001911](https://doi.org/10.1061/(asce)he.1943-5584.0001911).
- Huff, 1967. Time distribution rainfall in heavy storms. *Water Resour. Res.* 3 (4), 1007–1019.
- IPCC, 2023. Climate Change 2023: Synthesis Report. Contribution of Working Groups I, II and III to the Sixth Assessment Report of the Intergovernmental Panel on Climate Change. In: Core Writing Team, Lee, H., Romero, J. (Eds.), Intergovernmental Panel on Climate Change (IPCC), pp. 69–87. <https://doi.org/10.59327/IPCC/AR6-978929169164>.
- Johannsen, L.L., Schmaltz, E.M., Mitrovits, O., Klik, A., Smoliner, W., Wang, S., Strauss, P., 2022. An update of the spatial and temporal variability of rainfall erosivity (R-factor) for the main agricultural production zones of Austria. *Catena* 215. <https://doi.org/10.1016/j.catena.2022.106305>.
- Klik, A., Konecny, F., 2012. Rainfall erosivity in northeastern Austria. *Trans. ASABE* 56 (2), 719–725.
- Klik, A., Rosner, J., 2020. Long-term experience with conservation tillage practices in Austria: Impacts on soil erosion processes. *Soil Tillage Res.* 203 (December 2019), 104669 <https://doi.org/10.1016/j.still.2020.104669>.
- Klik, A., Haas, K., Dvorackova, A., Fuller, I.C., 2015. Spatial and temporal distribution of rainfall erosivity in New Zealand. *Soil Res.* 53 (7), 815. <https://doi.org/10.1071/SR14363>.
- Lai, C., Chen, X., Wang, Z., Wu, X., Zhao, S., Wu, X., Bai, W., 2016. Spatio-temporal variation in rainfall erosivity during 1960–2012 in the Pearl River Basin, China. *Catena* 137, 382–391. <https://doi.org/10.1016/j.catena.2015.10.008>.
- Lee, S., Bae, J.H., Hong, J., Yang, D., Panagos, P., Borrelli, P., Yang, J.E., Kim, J., Lim, K.J., 2022. Estimation of rainfall erosivity factor in Italy and Switzerland using Bayesian optimization based machine learning models. *Catena* 211, 105957. <https://doi.org/10.1016/j.catena.2021.105957>.
- Li, J., Xiong, M., Sun, R., Chen, L., 2023. Temporal variability of global potential water erosion based on an improved USLE model. *S2095633923000266 Int. Soil Water Conserv. Res.* <https://doi.org/10.1016/j.iswcr.2023.03.005>.
- Lloyd, S., 1982. Least squares quantization in PCM. *IEEE Trans. Inf. Theory* 28 (2), 129–137. <https://doi.org/10.1109/tit.1982.1056489>.
- Machado, R.L., Carvalho, D.F. de Costa, J.R., Neto, D.H. de O., Pinto, M.F., 2008. Analysis of rainfall erosivity associated to pluvial precipitation patterns in the Ribeirão das Lajes region, Rio de Janeiro state, Brazil. *Rev. Bras. De Cienc. Do Solo* 32 (5), 2113–2123. <https://doi.org/10.1590/S0100-06832008000500032>.
- Marzen, M., Iserloh, T., de Lima, J.L.M.P., Fister, W., Ries, J.B., 2017. Impact of severe rain storms on soil erosion: experimental evaluation of wind-driven rain and its implications for natural hazard management. *Sci. Total Environ.* 590–591, 502–513. <https://doi.org/10.1016/j.scitotenv.2017.02.190>.

- Matulla, C., Penlap, E.K., Haas, P., Formayer, H., 2003. Comparative analysis of spatial and seasonal variability: Austrian precipitation during the 20th century. *Int. J. Climatol.* 23 (13), 1577–1588. <https://doi.org/10.1002/joc.960>.
- MORAN, P.A.P., 1950. NOTES ON CONTINUOUS STOCHASTIC PHENOMENA. *Biometrika* 37 (1–2), 17–23. <https://doi.org/10.1093/biomet/37.1-2.17>.
- Mouton, J.P., Ferreira, M., Helberg, A.S.J., 2020. A comparison of clustering algorithms for automatic modulation classification. *Expert Syst. Appl.* 151, 113317 <https://doi.org/10.1016/j.eswa.2020.113317>.
- Nearing, M.A., Yin, S., Borrelli, P., Polyakov, V.O., 2017. Rainfall erosivity: An historical review. *CATENA* 157, 357–362. <https://doi.org/10.1016/j.catena.2017.06.004>.
- Nel, W., 2007. Intra-Storm Attributes of Extreme Storm Events in the Drakensberg, South Africa. *Physical Geography* 28 (2), 158–169. <https://doi.org/10.2747/0272-3646.28.2.158>.
- Nyssen, J., Vandenreyken, H., Poesen, J., Moeyersons, J., Deckers, J., Haile, M., Salles, C., Govers, G., 2005. Rainfall erosivity and variability in the Northern Ethiopian Highlands. *Journal of Hydrology* 311 (1–4), 172–187. <https://doi.org/10.1016/J.JHYDROL.2004.12.016>.
- Olefs, M., Formayer, H., Gobiet, A., Marke, T., Schöner, W., Revesz, M., 2021. Past and future changes of the Austrian climate – Importance for tourism. *J. Outdoor Recreat. Tour.* 34, 100395 <https://doi.org/10.1016/j.jort.2021.100395>.
- Padulano, R., Rianna, G., Santini, M., 2021. Datasets and approaches for the estimation of rainfall erosivity over Italy: a comprehensive comparison study and a new method. *J. Hydrol.: Reg. Stud.* 34, 100788 <https://doi.org/10.1016/j.ejrh.2021.100788>.
- Padulano, R., Santini, M., Mancini, M., Stojiljkovic, M., Rianna, G., 2023. Monthly to seasonal rainfall erosivity over Italy: Current assessment by empirical model and future projections by EURO-CORDEX ensemble. *CATENA* 223, 106943. <https://doi.org/10.1016/j.catena.2023.106943>.
- Panagos, P., Katsoyiannis, A., 2019. Soil erosion modelling: the new challenges as the result of policy developments in Europe. *Environ. Res.* 172 (February), 470–474. <https://doi.org/10.1016/j.envres.2019.02.043>.
- Panagos, P., Imeson, A., Meusburger, K., Borrelli, P., Poesen, J., Alewell, C., 2016. Soil conservation in Europe: wish or reality? *Land Degrad. Dev.* 27 (6), 1547–1551. <https://doi.org/10.1002/ldr.2538>.
- Papalexiou, S.M., Montanari, A., 2019. Global and regional increase of precipitation extremes under global warming. *Water Resour. Res.* 55 (6), 4901–4914. <https://doi.org/10.1029/2018WR024067>.
- Parsons, A.J., Stone, P.M., 2006. Effects of intra-storm variations in rainfall intensity on interrill runoff and erosion. *Catena* 67 (1), 68–78. <https://doi.org/10.1016/j.catena.2006.03.002>.
- Peng, T., Wang, S., 2012. Effects of land use, land cover and rainfall regimes on the surface runoff and soil loss on karst slopes in southwest China. *CATENA* 90, 53–62. <https://doi.org/10.1016/j.catena.2011.11.001>.
- Peng, X., Dai, Q., 2022. Drivers of soil erosion and subsurface loss by soil leakage during karst rocky desertification in SW China. *Int. Soil Water Conserv. Res.* 10 (2), 217–227. <https://doi.org/10.1016/j.iswcr.2021.10.001>.
- Renard, K.G., Foster, G.R., Weesies, G.A., Porter, J.P., 1991. RUSLE: revised universal soil loss equation. *J. Soil Water Conserv.* 46 (1), 30–33.
- Riquetti, N.B., Mello, C.R., Beskow, S., Viola, M.R., 2020. Rainfall erosivity in South America: Current patterns and future perspectives. *Sci. Total Environ.* 724, 138315 <https://doi.org/10.1016/j.scitotenv.2020.138315>.
- Rogler, H., Schwertmann, U., 1981. Erosivität der Niederschläge und Isoerodentkarte von Bayern. *Z. für Kult. und Flurberein.*
- Schmalz, E.M., Krammer, C., Dersch, G., Weinberger, C., Kuderna, M., Strauss, P., 2023. The effectiveness of soil erosion measures for cropland in the Austrian Agri-environmental Programme: a national approach using local data. *Agric. Ecosyst. Environ.* 355 (May), 108590 <https://doi.org/10.1016/j.agee.2023.108590>.
- Schmidt, S., Alewell, C., Panagos, P., Meusburger, K., 2016. Regionalization of monthly rainfall erosivity patterns in Switzerland. *Hydrol. Earth Syst. Sci.* 20 (10), 4359–4373. <https://doi.org/10.5194/hess-20-4359-2016>.
- Schroeder, K., Kirchengast, G., 2018. Sensitivity of extreme precipitation to temperature: the variability of scaling factors from a regional to local perspective. *Clim. Dyn.* 50 (11–12), 3981–3994. <https://doi.org/10.1007/s00382-017-3857-9>.
- Seibert, P., Frank, A., Formayer, H., 2007. Synoptic and regional patterns of heavy precipitation in Austria. *Theor. Appl. Climatol.* 87 (1–4), 139–153. <https://doi.org/10.1007/s00704-006-0198-8>.
- Strauss, P., Auerswald, K., Klaghofer, E., Blum, W.E.H., 1995. Rainfall Erosivity: A Comp. Austria-Bavaria.
- Strohmeier, S., Laaha, G., Holzmann, H., Klik, A., 2015. Magnitude and occurrence probability of soil loss: a risk analytical approach for the plot scale for two sites in Lower Austria. *Land Degrad. Dev.* 27 (1), 43–51. <https://doi.org/10.1002/ldr.2354>.
- Syakur, M.A., Khotimah, B.K., Rochman, E.M.S., Satoto, B.D., 2018. Integration K-means clustering method and elbow method for identification of the best customer profile cluster. *IOP Conf. Ser.: Mater. Sci. Eng.* 336 (1) <https://doi.org/10.1088/1757-899X/336/1/012017>.
- Van Dijk, A.I.J.M., Bruijnzeel, L.A., Rosewell, C.J., 2002. Rainfall intensity-kinetic energy relationships: A critical literature appraisal. *J. Hydrol.* 261 (1–4), 1–23. [https://doi.org/10.1016/S0022-1694\(02\)00020-3](https://doi.org/10.1016/S0022-1694(02)00020-3).
- Wang, W., Yin, S., Xie, Y., Liu, B., Liu, Y., 2016. Effects of four storm patterns on soil loss from five soils under natural rainfall. *Catena* 141, 56–65. <https://doi.org/10.1016/j.catena.2016.02.019>.
- Wang, W., Yin, S., He, Z., Chen, D., Wang, H., Klik, A., 2023. Projections of rainfall erosivity in climate change scenarios for mainland China. *Catena* 232, 107391. <https://doi.org/10.1016/j.catena.2023.107391>.
- Wischmeier, W.H., Smith, D.D., 1958. Rainfall energy and its relationship to soil loss. *Eos Trans. Am. Geophys. Union* 39 (2), 285–291. <https://doi.org/10.1029/TR039i002p00285>.
- Yang, P., Li, R., Gu, Z., Qin, L., Song, T., Liu, Z., Gao, J., Yuan, J., 2022. Runoff sediment characteristics affected by erosive rainfall patterns in a small watershed in karst areas of southwest China. *Catena* 219, 106591. <https://doi.org/10.1016/j.catena.2022.106591>.
- Yin, S., Nearing, M.A., Borrelli, P., Xue, X., 2017. Rainfall erosivity: an overview of methodologies and applications. *Vadose Zone J.* 16 (12), 1–16. <https://doi.org/10.2136/vzj2017.06.0131>.
- Yue, Z., Xiong, L., Zha, X., Liu, C., Chen, J., Liu, D., 2022. Impact of thresholds on nonstationary frequency analyses of peak over threshold extreme rainfall series in Pearl River Basin, China. *Atmos. Res.* 276 (May), 106269 <https://doi.org/10.1016/j.atmosres.2022.106269>.